Aerosol-Jet-Assisted Thin-Film Growth of $CH_3NH_3PbI_3$ Perovskites—A Means to Achieve High Quality, Defect-Free Films for Efficient Solar Cells

Santanu Bag, James R. Deneault, and Michael F. Durstock**

A high level of automation is desirable to facilitate the lab-to-fab process transfer of the emerging perovskite-based solar technology. Here, an automated aerosol-jet printing technique is introduced for precisely controlling the thin-film perovskite growth in a planar heterojunction p–i–n solar cell device structure. The roles of some of the user defined parameters from a computer-aided design file are studied for the reproducible fabrication of pure $CH_3NH_3PbI_3$ thin films under near ambient conditions. Preliminary power conversion efficiencies up to 15.4% are achieved when such films are incorporated in a poly(3,4-ethylenedioxythiophene):polystyrene sulfonate-perovskite-phenyl-C71-butyric acid methyl ester type device format. It is further shown that the deposition of atomized materials in the form of a gaseous mist helps to form a highly uniform and PbI_2 residue-free $CH_3NH_3PbI_3$ film and offers advantages over the conventional two-step solution approach by avoiding the detrimental solid–liquid interface induced perovskite crystallization. Ultimately, by integrating full 3D motion control, the fabrication of perovskite layers directly on a 3D curved surface becomes possible. This work suggests that 3D automation with aerosol-jet printing, once fully optimized, could form a universal platform for the lab-to-fab process transfer of solution-based perovskite photovoltaics and steer development of new design strategies for numerous embedded structural power applications.

1. Introduction

Disruptive photovoltaic (PV) technologies that imitate the principles of digital printing as a means of manufacturing devices offer the promise of low cost along with the advantages of unique form factors and high throughput processing.[1] Inorganic–organic hybrid, perovskite-based thin-film photovoltaics is a relatively new technology, but it has quickly become a highly impressive contender in this exciting field, underpinned by several unprecedented characteristics including high certified device efficiencies, low temperature solution processability, and mechanical flexibility.[2,3] Additionally, they are light weight, comprised of earth-abundant materials, and are chemically tunable. To date, most demonstrations of this technology are limited to lab scale and based on an extremely labor intensive manual spin-coating process in an inert atmosphere.[4] In order to drive the technology beyond the academic environment and to facilitate further development for commercialization, significant research efforts focused on the "lab-to-fab" translation of the fabrication methods are needed.[5,6] Unfortunately, the transfer of device results derived from spin-coated photoactive layers in a standard laboratory setup to fabrication level devices is nontrivial due to the enormous complexity of the thin-film perovskite growth dynamics[7] and the lack of a generic protocol for fabricating high quality, high performing films, which would ultimately lead to efficient solar cell devices. Indeed, the active layer's morphology critically influences its optoelectronic properties and, in turn, the overall device PV performance.[8,9] Furthermore, the optimized perovskite solar cell performances for lab scale, spin-coated devices tend to be highly technique sensitive as a result of the different mechanisms that drive the active layer film formation.

In this work, a method for shifting perovskite solar cell fabrication away from the benchtop toward a more automated, reproducible, and potentially scalable fabrication approach is investigated. While there has been some work reported in fabricating perovskite solar cells using doctor-blading,[10,11] spray-coating,[12–14] inkjet-printing,[15] and slot-die coating,[5,16,17] few have focused on aerosol-jet deposition technology. It is shown here that aerosol-jet deposition technology is well suited to deal with the challenges associated with precisely controlling the film morphology, composition, and yield in a fully automated and reproducible way. Furthermore, aerosol-jet deposition shows a great deal of promise toward the manufacture of uniform, large-grained, high-quality, defect-free perovskite films that possess the fidelity necessary for commercial relevance.[18]

Dr. S. Bag, J. R. Deneault, Dr. M. F. Durstock
Materials and Manufacturing Directorate
Air Force Research Laboratory
Wright-Patterson Air Force Base
OH 45433-7702, USA
E-mail: santanu.bag.ctr.in@us.af.mil; michael.durstock@us.af.mil
Dr. S. Bag
National Research Council
Washington, D.C. 20001, USA
J. R. Deneault
Universal Technology Corporation
Beavercreek, OH 45432, USA

DOI: 10.1002/aenm.201701151

For this work, the perovskite precursor inks are atomized using ultrasonic transduction. Here, high-frequency acoustic waves are passed through a small volume (≤1 mL) of the ink and effect a capillary cresting phenomenon at the surface of the ink where very fine (1–2 µm) droplets are emitted. The head space above the ink quickly fills with a dense aerosol which is subsequently picked up and delivered to the nozzle by a controlled flow of an inert 'carrier' gas (nitrogen). At the nozzle, a second gas flow is introduced coaxial to the carrier gas. This "sheath" flow acts to constrict and collimate the flow of ink-entrained carrier gas such that features much smaller than the nozzle orifice diameter are produced on the substrate.

Predefined computer-aided design (CAD)-generated tool paths are executed to realize a fully automated thin-film deposition routine in which 2D or 3D motion control can be achieved and the aerosol can be deposited as defined at any given position in a digital manner.[19] Parameters such as gas flow rate, print speed, x–y–z motion, and ink and build platen temperatures can be easily defined within the tool path. This affords a mask-free, digital and potentially scalable thin-film deposition method with minimal waste of starting material and high throughput as compared to the traditional spin casting motif. Aerosol-jet deposition also opens up possibilities for additive manufacturing of thin-film layer stacks on any arbitrary 3D surface without cutting or assembling steps.[19] Additionally, the noncontact solvent-free nature and "jet-on demand" control of the aerosol-jet printing (AJP) are advantageous for mitigating defects in multilayer deposition.

In order to explore the effectiveness and reliability of this approach in fabricating inorganic–organic hybrid perovskite films, AJP was used as a deposition technique to fabricate methylammonium lead tri-iodide ($CH_3NH_3PbI_3$)-based single halide films on a low-temperature-processed poly(3,4-ethylenedioxythiophene):polystyrene sulfonate (PEDOT:PSS) surface under near ambient conditions. In this preliminary work, power conversion efficiencies up to 15.4% have been achieved from these aerosol-jet printed thin perovskite films using a PEDOT:PSS-perovskite-phenyl-C71-butyric acid methyl ester (PCBM) device configuration through comprehensive print optimization on a planar surface. Direct printing of perovskite layers by aerosol-jet deposition on a curved hemispherical surface is also presented, and efficiencies of ≈5.4% are achieved using the same planar heterojunction (PHJ) device layout after conforming to a flat surface. To the best of the authors' knowledge, this is the first report demonstrating programmable fabrication of perovskite solar cells on a curved surface using a direct printing approach. The results highlight that fully automated, CAD-controlled aerosol-jet printing is not only a promising option for the "lab-to-fab" process transfer of the solution-processed perovskite PV technology, but could also be a viable method for integrating these solar cells directly onto any arbitrary 3D substrate/structure.

2. Results and Discussion

2.1. Perovskite Conversion at Mist–Solid Interface

Figure 1a shows a schematic illustration of the aerosol-jet deposition system that was used to print the perovskite active layer. Here, the "hands-free" nature of this method is evident; the deposition of each of the precursor components can be automated, avoiding menial and manual process optimization steps as commonly practiced using spin-coating processes. The system can be simplified to five main components; (i) the ultrasonic atomizer source, (ii) the print head, (iii) the motion stage, (iv) flow controllers, and (v) motion controllers.

The ultrasonic atomizer source (i) is comprised of a temperature-controlled ink reservoir with an integrated ultrasonic transducer. This is where the aerosol is generated and entrained into the carrier gas. The print head (ii) contains the print nozzle assembly and the process shutter and is capable of motorized motion along the z-axis. Since the response time of the flow of aerosol-entrained gas is very slow (30–300 s for steady state) an integrated process shutter is employed as a switchable physical barrier to effectively turn on and off deposition. Introduction of the sheath gas and aerosol collimation occurs within the print nozzle assembly where both the ink-entrained carrier gas and sheath gas flows are coaxially combined. Mounted on the x and y motion stages (iii) is a heated vacuum platen where substrates can be translated with high accuracy beneath the nozzle. Flow controllers (iv) and motion controllers (v) utilize PID feedback to accurately deliver gas flow rates and motion, respectively, as dictated by the user and/or tool path. The whole set up is fully automated so that the movements of the substrate and print head, gas flow rates, atomization intensity, temperatures, and shutter operation can be precisely managed to make fabrication consistent and reliable across different regions and multiple devices. Tool paths to produce desired printing features can be generated either by AutoCAD drawings or by manual programming.

The AJP system offers the operator a wider control over process parameters thus enabling greater flexibility in film fabrication and device layout. Initial studies were aimed at first-order optimization of deposition conditions in order to establish a general protocol for perovskite film formation. Here, films of $CH_3NH_3PbI_3$ were fabricated as a model for the hybrid perovskite photoactive layer to investigate the aerosol-solid crystallization process between two precursor components, PbI_2 and CH_3NH_3I. Film morphology, chemical composition, and grain boundaries in the films were scrutinized systematically to generate a controllable approach for mitigating defects in a sequential deposition process under near ambient conditions. To date, sequential deposition of precursors is the most widely used method to fabricate perovskite layers.[9] In this work, the sequential deposition approach was preserved but also augmented by incorporating the full system automation and noncontact nature of the aerosol-jet printer. Here, a methyl ammonium iodide (MAI, CH_3NH_3 I) aerosol mist is generated from its precursor ink using the ultrasonic atomizer and subsequently jetted onto a PbI_2 film using preprogrammed deposition routines. The process steps are illustrated in Figure 1b. First, a thin film of PbI_2 is deposited onto a PEDOT:PSS-coated glass/indium-doped tin oxide (ITO) substrate using either spin casting or AJP. The precise conversion of the solid PbI_2 layer to $CH_3NH_3PbI_3$ is achieved via an in situ solid–mist–solid-phase transformation process. The detailed film deposition and device fabrication process are described in the Experimental Section. Briefly, a commercial PEDOT:PSS is spin cast onto a glass/ITO surface to form a hole transport layer (HTL). For morphological

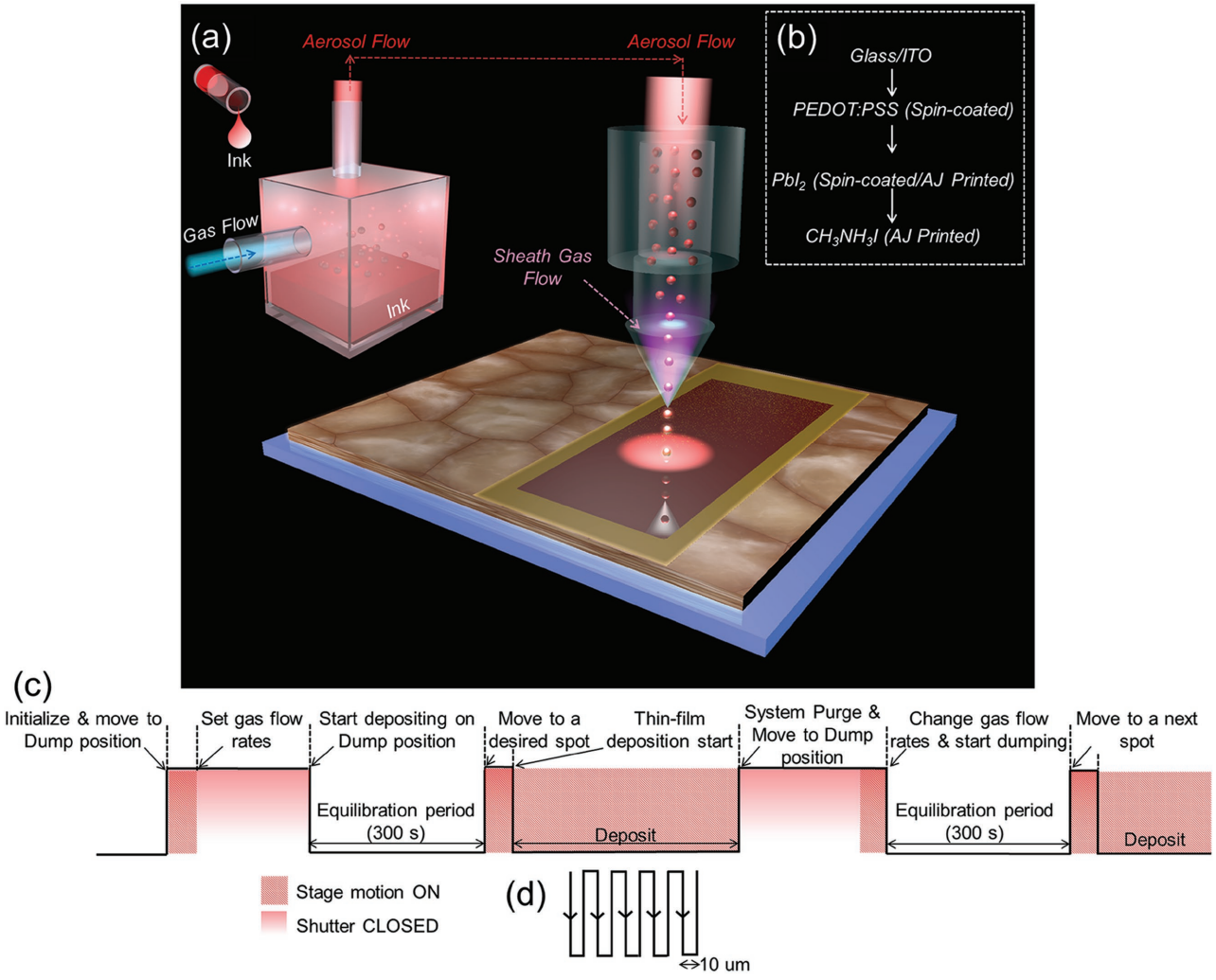

Figure 1. a) Simplified diagram for the core parts of the aerosol-jet (AJ) printer used in this study for perovskite thin-film growth. The key parameters optimized in this work are ink formulation, atomizer flow rate, and sheath flow rate. b) Schematic representation of the process flow used to form $CH_3NH_3PbI_3$ perovskite films in a p–i–n type planar heterojunction device structure. c) Timing diagram for the present AJ operation. d) Direction of the AJ print-head movement relative to the substrate for producing individual rectangular shaped perovskite "pixels" of predefined size. Patterns are produced using a nozzle with a diameter of 150 µm at a fixed platen temperature.

evolution studies, a solution of PbI_2 in *N,N*-dimethylformamide (DMF) is subsequently spin-cast on top of the HTL where variations of the desired PbI_2 film morphologies are achieved by drying the wet PbI_2 film at varying rates (5 min for compact PbI_2 and 12 min for nanoporous PbI_2 layer) immediately after spin-casting. Next, the solid PbI_2 layer is converted to $CH_3NH_3PbI_3$ by introducing MAI in aerosol form from the AJP system. The timing diagram in Figure 1c summarizes a series of automated processes demonstrating how the atomized ink is patterned at predefined locations onto the substrate. Patterning is achieved using x/y motion control stages, which move the substrate at a velocity of 30 mm s^{-1} under a (laterally) fixed nozzle. For this work, ≈50 µm traces are deposited in a 10 µm pitch raster pattern (Figure 1d) in order to fill predefined square/rectangular areas referred to herein as "pixels." At low temperature annealing conditions, these overlapping traces coalesce to form a continuous film.

The aerosol jet deposition approach, which is novel for perovskite film growth, precludes many of the detrimental events (e.g., the formation of the needle forming solvated $CH_3NH_3PbI_3$.DMF intermediate phase, dissolution of film etc.) commonly observed in conventional solution-based perovskite deposition processes.[20] This is likely due to the exquisite control afforded by this technique in precisely depositing metered quantities of perovskite precursors in the form of an aerosol mist such that grain growth, perovskite conversion, and final film morphology can be parametrically controlled. It will be shown in the following sections that the thin-film microstructural features are tunable simply by adjusting some of the common parameters (i.e., atomizer and sheath gas flow rates) in the AJP system.

In order to effectively atomize and deposit MAI using AJP, an appropriate formulation having the desired rheology, volatility, and concentration was established where 2 wt% MAI was

combined with a 1:3 (v/v) mixture of iso-propanol (IPA) and DMF. Here, the MAI "ink" was deposited on spin-cast films of PbI_2 and the atomizer and sheath gas flow rates were systematically varied. The compositional and morphological evolution of the perovskite was monitored using a series of X-ray diffraction (XRD) and scanning electron microscopy (SEM) measurements to elucidate the aerosol-solid crystallization process. This study took place in air at 70 °C with a relative humidity of <30%. Here, the atomizer flow rate (AFR) was increased progressively from 10 standard cubic centimeter per minute (sccm) to 25 sccm in 5 sccm increments, and the sheath flow rate (SFR) was swept from 5 to 35 sccm in 10 sccm increments. In order to isolate the effects of varying these flow rates, all parameters of the AJP system were kept fixed throughout the printing process.

Figure 2a shows top-view SEM images of the PbI_2 film after aerosol jet deposition of MAI (see zoomed out images in Figure S1, Supporting Information). These images reveal morphological variations for different gas flow rates and clearly demonstrate that film morphology is largely dependent on both the AFR and the SFR. The PbI_2 layer (≈240 nm) used here has a compact bulk morphology with a somewhat spiny and wart-like surface texture, which is formed by drying the wet PbI_2 naturally for 5 min after spin-coating followed by rapid thermal quenching. Figure 2b shows optical images of the printed perovskite films after aerosol jet deposition of MAI for various jetting conditions. For samples where MAI was deposited using an AFR of 10 sccm there is arguably no visible change in film texture (the bottom most row). This is likely due to an extremely low deposition rate for these flow settings. However, as the AFR increases the PbI_2 film color changes from light yellow to brown and ultimately to dark brown suggesting a gradual conversion of PbI_2 to perovskite.[21]

To further understand these findings, X-ray diffraction data were collected and is shown in Figure 2c. While the optical micrographs indicate some conversion of PbI_2 to perovskite in a diffused form at an AFR of 15 and a SFR of 5 (pixel ⑤), the perovskite concentration only reaches X-ray detection limits beginning in pixel ⑦. The diffraction peaks at 2θ of 12.7°, 25.5°, and 38.6°, indicative of the hexagonal lattice of PbI_2, are still predominant in the film.[22] Increasing the SFR further towards 35 sccm with the same 15 sccm AFR slowly increases the perovskite content in the film, and the diffused pattern is gradually converted to more discrete ones. Consequently, the characteristic (110), (220), and (330) diffraction peaks of the 3D tetragonal perovskite phase at 2θ of 14.1°, 28.4°, and 43.1° become stronger and sharper.[22] In pixel ⑩, at an AFR of 20 sccm and a SFR of 15 sccm, a complete conversion of PbI_2 to $CH_3NH_3PbI_3$ with full coverage is observed on the top film surface by SEM (see angle- dependent grazing incidence X-ray diffraction data in Figure S2, Supporting Information); however, the XRD data show the presence of PbI_2 phase in the bulk of the film. Jetting

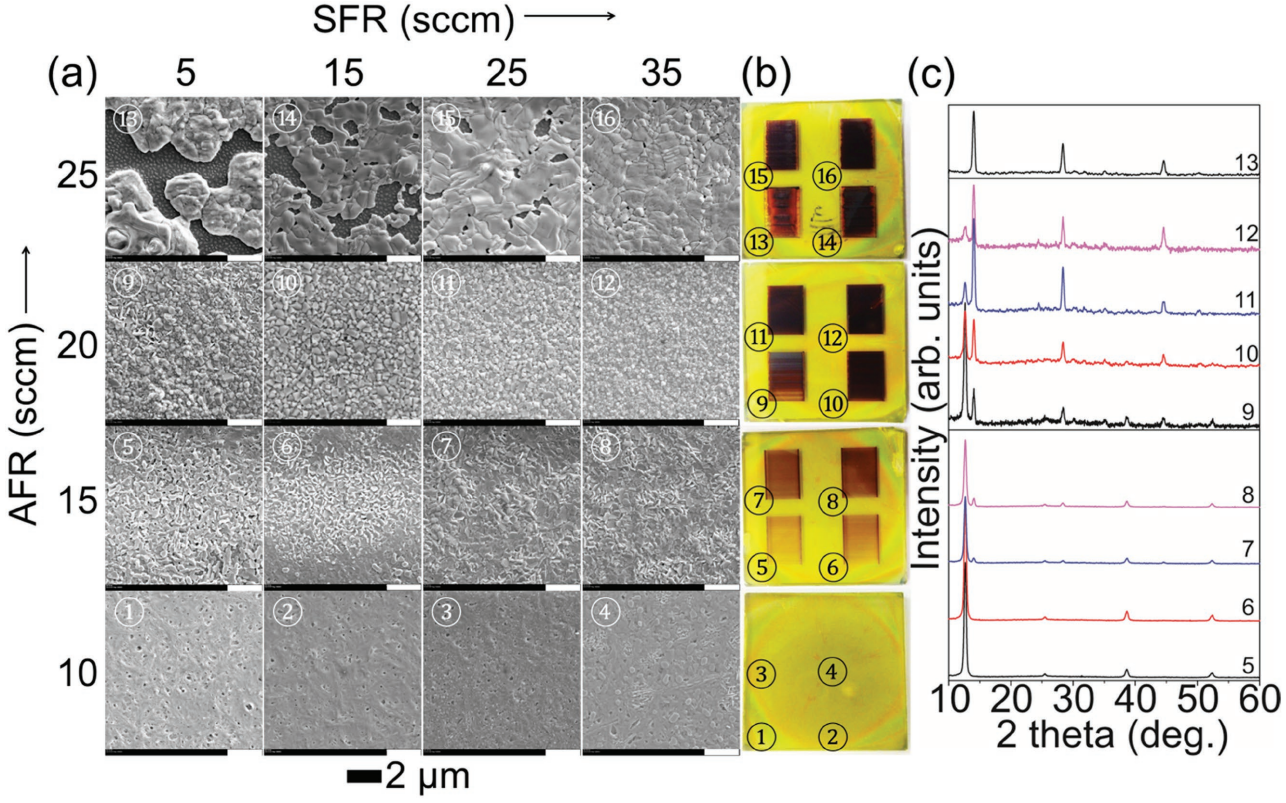

Figure 2. a) Top-view SEM images of the 350 nm perovskite films grown on glass/ITO/PEDOT:PSS with a compact PbI_2 layer, under variable AJ printing conditions. Films are annealed at 100 °C for 80 min with DMF vapor after printing. In all images, scale bars are 2 μm. b) Digital photographs of the corresponding printed $CH_3NH_3PbI_3$ films on 1 in. × 1 in. square substrates. c) Comparison of XRD patterns of the AJ printed films.

at a higher SFR results in improved perovskite conversion, but concomitant decrease in average grain size from 300 nm in pixel ⑩ to 200 nm in pixel ⑪ and ultimately to 140 nm in pixel ⑫ (see Figure S3 in the Supporting Information). Complete consumption of the PbI_2 peak is noticed in the XRD pattern at 25 sccm AFR (pixel ⑬). Unfortunately, at this high AFR the film suffers from extremely poor surface coverage, which could be detrimental to its use in device level optimization. Upon further increase in the SFR, a small improvement of the film coverage is noticeable at some localized positions and a set of strong peaks arising from the tetragonal perovskite phase is still detected.

The UV–vis absorption spectra of the films in Figure 2b are displayed in **Figure 3**a. Irrespective of the SFR, all the films prepared at low atomization flow rates (AFR of 10 and 15 sccm) exhibit a strong light absorption in the UV-blue range with a cut-off edge at ≈510 nm corresponding to PbI_2.[23] The absorption intensity is enhanced when the AFR is increased to 20 sccm and upon further rise in the SFR the sharp band-edge region gradually broadens across the visible region with a shoulder at 800 nm, which indicates the formation of perovskite.[23] However, as the AFR increases from 20 to 25 sccm, pinholes and uncovered glass/ITO/PEDOT:PSS surfaces begin to appear, which ultimately results in full transmission of light through the uncovered regions of the substrate. The evaluation of the absorbance at 720 nm versus flow rates is shown in Figure 3b and reveals its progressive rise with increasing flow rates indicating perovskite conversion. In addition, the gradual transformation of PbI_2 to perovskite provides longer carrier lifetimes as analyzed by the time-resolved photoluminescence (TRPL) decay curves of the printed samples on glass (see Figure S4 and Table S1 in the Supporting Information).

These results demonstrate general trends related to hybrid perovskite formation at the mist–solid interface, and how the thin-film morphology can be engineered by manipulating the gas flow rates of the AJP system. These are summarized and briefly illustrated through a series of simple sketches in

Figure 4. Three different AFR test conditions, low (left column), medium (middle column), and high (right column), are highlighted in this scheme. At low AFRs and SFRs, only a very small amount of MAI aerosol is carried to the nozzle and low levels of aerodynamic focusing are achieved. These conditions produce a diffuse cloudy appearance on the PbI_2 film with almost no perovskite conversion. When the SFR is increased, the aerosol stream becomes more focussed and aerosol droplets are better able to coalesce, accumulate, and penetrate the PbI_2 film as they reach the surface. However, at lower AFRs, only limited quantities of the MAI mist are supplied resulting in noncontiguous deposition. As such, perovskite conversion is intermittent and irregular. With a moderate AFR, while increasing the SFR, the PbI_2 films are gradually converted to the $CH_3NH_3PbI_3$ perovskite phase with full surface coverage, augmented by a serial change in the average grain size. Here with a gradual increase in the SFR, initially, grains with less pronounced boundaries are formed, which then change to polygonal forms with distinct boundaries and ultimately to smaller grains. This may be due to the rapid drying of the aerosol mist and accelerated nucleation of perovskite on the PEDOT:PSS after the chemical reaction between solid PbI_2 and MAI aerosol mist with increased SFR. Finally, depositing MAI mist at high AFR causes partial dissolution of the underlying PbI_2 film as higher deposition rates result in pooling of the ink on the surface of the PbI_2 film. Although this ensures complete conversion of PbI_2 to $CH_3NH_3PbI_3$, it redistributes the PbI_2 resulting in nonuniform and incomplete perovskite film coverage. Therefore, only at moderate atomizer and sheath flow rates the appropriate balance between film morphology and perovskite conversion can be accomplished.

Having established a general understanding on the perovskite film formation process at the mist–solid interface by AJP, we seek to study how the morphology of the PbI_2 layer influences the crystallization of $CH_3NH_3PbI_3$. It has been documented by other researchers in this field that for a two-step sequential deposition scheme, the conversion and morphology

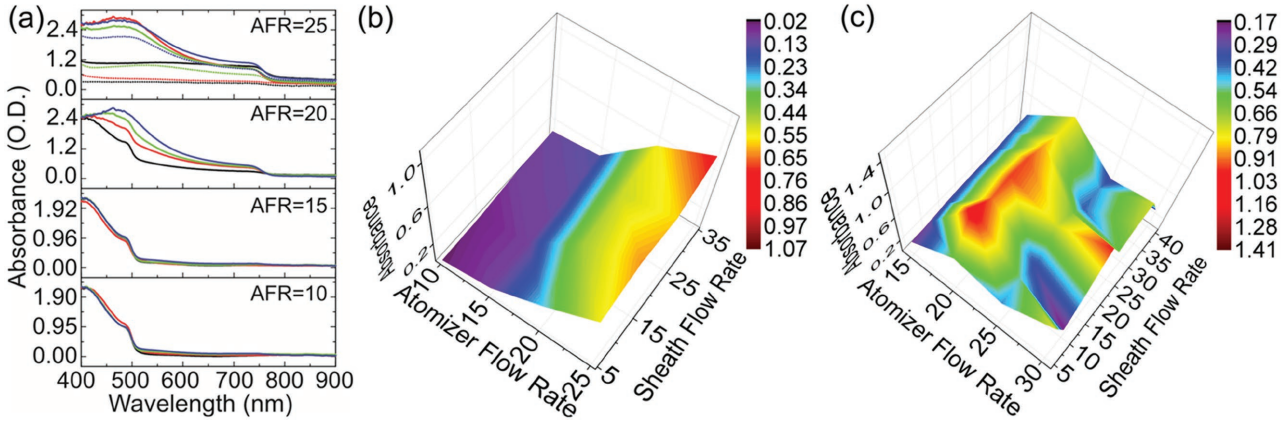

Figure 3. a) UV–vis absorption spectra of the AJ printed perovskite films based on the conditions as shown in Figure 2 (black line: SFR = 5, red line: SFR = 15, green line: SFR = 25, blue line: SFR = 35; all flow rates are in sccm unit). At a higher atomization flow rate (i.e., 25 sccm), films become noncontinuous, which leads to uneven light absorption across film (dotted lines imply measurements on different areas of the sample). 3D views for evolution of UV–vis absorbance at 720 nm wavelength as a function of AFR and SFR made from b) compact PbI_2 and c) nanoporous PbI_2 layers. All flow rates are in sccm unit and absorbances are in O.D.

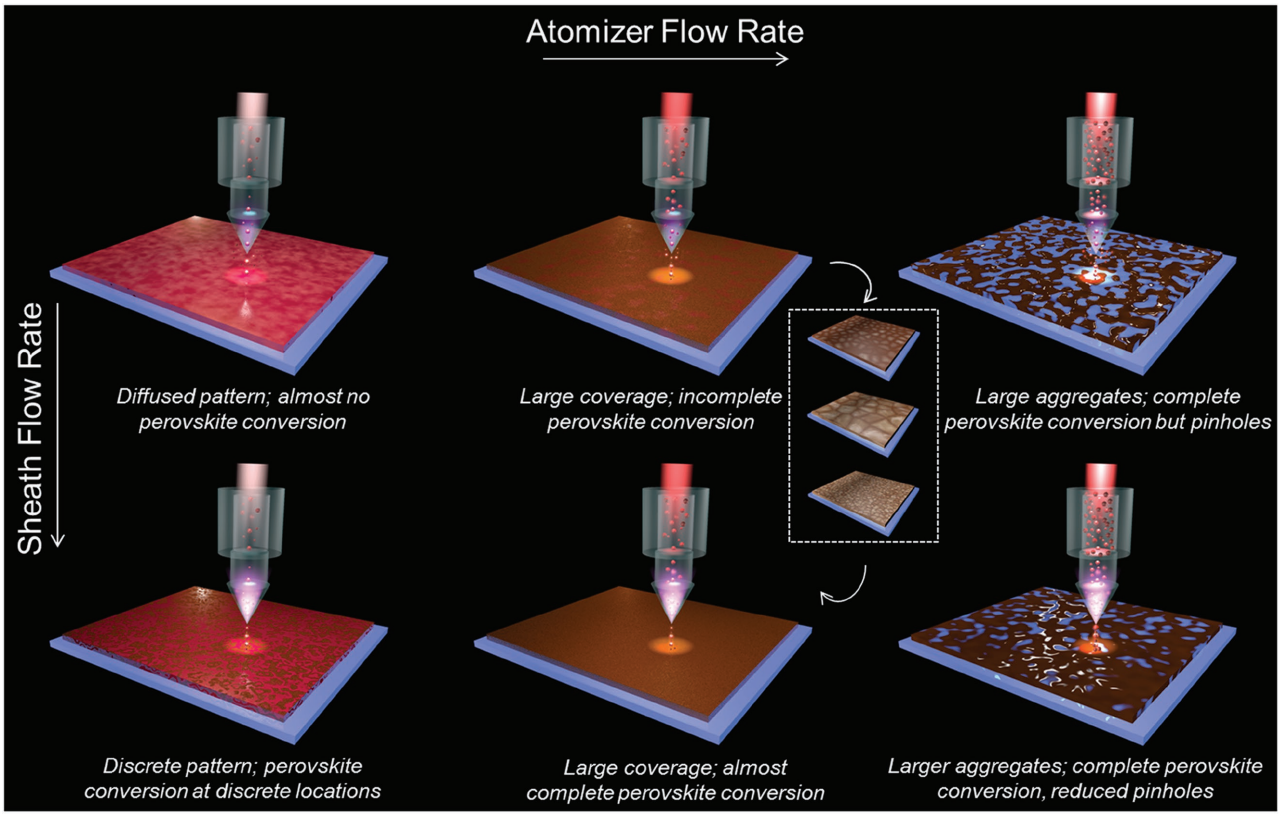

Figure 4. An illustration of perovskite formation and evolution of film morphology under different AFR and SFR during aerosol-jet printing.

of the final perovskite film is strongly dependent on the initial quality of PbI_2 layer.[5,23–25] A diffusion-facilitated support medium enables efficient transport of MAI into the bulk of PbI_2 layer, leading to its rapid and high conversion to $CH_3NH_3PbI_3$. As opposed to the compact PbI_2 layer, investigated initially in this study, we now explore the use of nanoporous PbI_2 for the evolution of perovskite by AJP. These nanoporous PbI_2 layers were generated by simply increasing the PbI_2 drying time after its deposition by spin-coating (see methods in experimental section). SEM surface images in **Figure 5** and Figure S5 (Supporting Information) show (gas) flow rate-dependent controlled transformation of nanoporous PbI_2 to perovskite and reveal similar trends of continuous conversion of PbI_2 to $CH_3NH_3PbI_3$ with increasing gas flow rates as observed for the compact PbI_2 layer (Figure 3c). A notable difference, however, is the formation of larger size perovskite grains from nanoporous PbI_2 at a medium flow rate (AFR: 20 sccm, SFR: 10 sccm). No PbI_2 impurity phase is detected in the XRD pattern confirming complete conversion of PbI_2 to $CH_3NH_3PbI_3$. Using identical AJP parameters, the average grain size substantially increases from ≈300 to ≈800 nm (see Figures S3a and S6 in the Supporting Information) after switching to nanoporous PbI_2 from compact PbI_2. While the growth of such large grains could benefit the charge transport properties of the perovskite film, it accompanies small crevices in the film and thus could reduce the shunt resistance of fabricated planar solar cell devices. Here in the porous PbI_2 layer, $CH_3NH_3PbI_3$ grows three dimensionally due to facile diffusion of ions, which creates variable size gaps between adjacent $CH_3NH_3PbI_3$ grains. Therefore, the results in Figure 5 imply that if the formation of these gaps and crevices can be mitigated, an AFR of 20 sccm with a SFR of around 10–15 sccm on a nanoporous PbI_2 surface is likely to be the most promising printing condition to fabricate high quality perovskite films suitable for efficient solar cell devices.

Our previous study demonstrated that the introduction of a controlled amount of mobile sodium ions into a diffusion facilitated support medium during the crystallization of perovskite helps to grow continuous films with large, micron-size crystallite domains.[26] It is believed that very low concentrations of sodium play dual roles in thin-film perovskite growth. These serve as nucleating sites in the course of crystallization and also help to facilitate grain-boundary mobility during thermal processing steps. Here, we adopt the same additive assisted grain growth strategy to fill up the small voids in the AJ printed film (Figure 5, AFR: 20 sccm and SFR: 10–15 sccm) with large grains. A small amount (2 mol%) of sodium iodide is added as an additive in the MAI formulation (in IPA:DMF) and is deposited on the nanoporous PbI_2 layer by the AJP system. The top-view SEM images of the perovskite films prepared from such a formulation with varied gas flow rates are presented in **Figure 6**a. It is seen that high quality, pinhole-free, and continuous perovskite films with larger grains (average grain size of ≈1 μm at AFR of 20–22 sccm and SFR of 10 sccm; see Figure S7 in the Supporting Information) can be obtained when NaI-containing MAI aerosol is deposited on nanoporous PbI_2 layers. The larger grain size also indicates improved

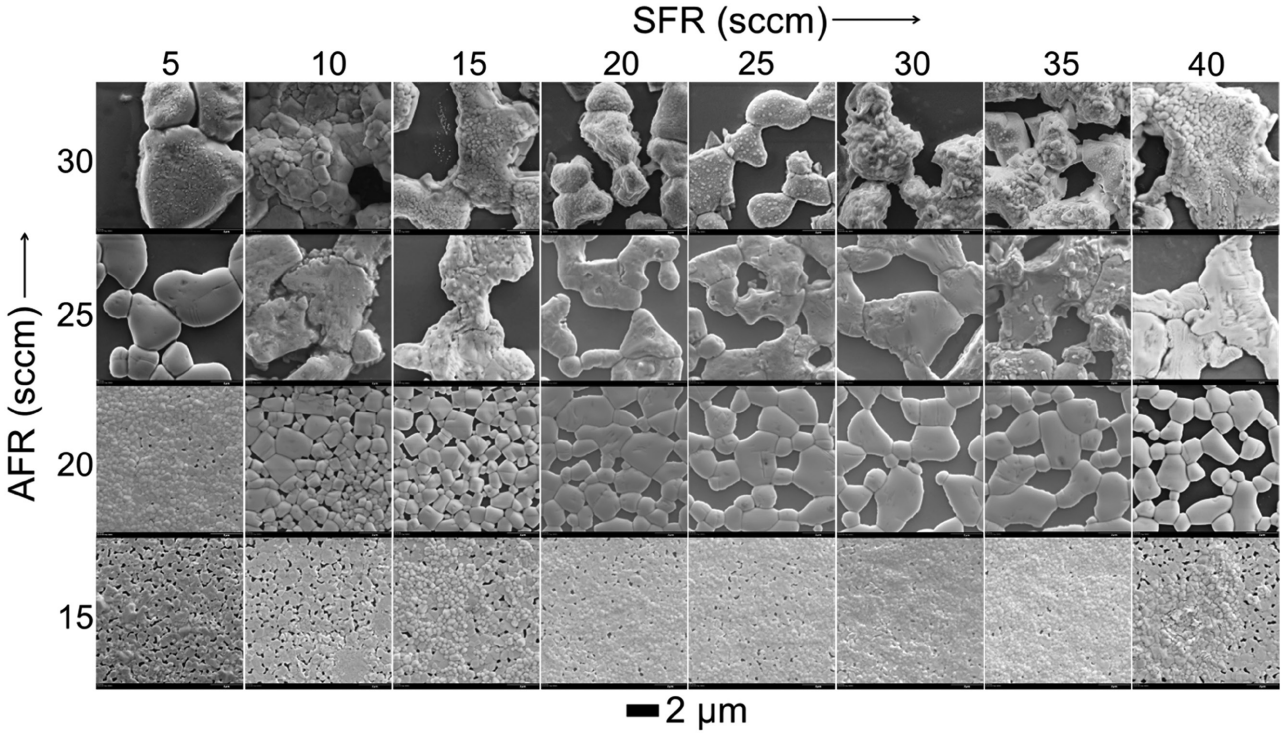

Figure 5. Top-view SEM images of the 350 nm perovskite films fabricated on glass/ITO/PEDOT:PSS surface from nanoporous PbI_2 layer at various AJ printing conditions. In all images, scale bars are 2 μm.

crystallization of the perovskite film, which is confirmed by the XRD pattern (Figure 6b). The crystal structure still follows that of the pristine tetragonal perovskite phase. However, compared to the pristine samples made without an additive, the intensity of the characteristic peaks corresponding to the tetragonal I4/mcm structure[22] increases significantly after the NaI addition. This suggests that the crystal grains in the $CH_3NH_3PbI_3$ perovskite films formed by this new additive assisted method are more oriented. TRPL measurements on these films further reveal longer average carrier lifetime (FigureS4 and Table S1, Supporting Information).

From the results shown above, it is feasible to fabricate pinhole-free, highly uniform, high-purity, and large-grained thin perovskite films with desirable optoelectronic properties using a hands-off automated approach. Nevertheless, successful automated fabrication requires optimized AJP conditions, proper ink formulation, and the right seed layer, e.g., compact/nanoporous PbI_2.

2.2. Photovoltaic Application

To quantify the optoelectronic performance of the perovskite layers crystallized at the mist–solid interface with the help of AJP, various films have been subsequently integrated into a p–i–n type PHJ solar cell device with a glass/ITO/PEDOT:PSS/$CH_3NH_3PbI_3$/$PC_{71}BM$/C_{60}/Al architecture (**Figure 7**a) and tested.[26] Since voids in perovskite films have already been shown to cause shorting in thin-film PV devices resulting in diminished performance,[2,8] this work will focus instead on a comparison of two different pinhole-free perovskite device paradigms toward PHJ device applications; (1) films with small grains prepared from a compact PbI_2 layer without NaI additive (representative sample in Figure 2, pix ⑫), and (2) films with large grains prepared from a nanoporous PbI_2 layer with NaI additive (representative top-view SEM image of the film in Figure 6). The performance characteristics of the fabricated solar cell devices are measured by the current density (J)–voltage (V) curves under light intensities of 100 mW cm^{-2}. Among all the devices, the highest power conversion efficiency (PCE) achieved was due to the additive enhanced crystallization of a pinhole-free, large grained perovskite active layer. A champion cell exhibiting an outstanding PCE of 15.4% with an impressive fill factor (FF) of 76%, a short-circuit current density (J_{sc}) of 21 mA cm^{-2} and an open-circuit voltage (V_{oc}) of 0.96 V, is obtained when NaI is used to induce larger grain sizes and mitigate defects in perovskite films for photovoltaic cells (Figure 7b, Figure S8, Supporting Information). On the other hand, in the case of additive free fabrication of pinhole-free perovskites, the highest PCE reaches 11.6%, which is considerably lower in performance than the additive based one. Here, all the photovoltaic device parameters including FF, J_{sc}, and V_{oc} are dramatically reduced resulting in an overall decrease in device PCE. Consistent with the performance characteristics of the best cells, the statistical distribution of the PCE for more than 50 devices, each made with and without additive, follows a similar trend as shown in Figure 7c. The hysteresis in all of our fabricated devices is negligible, which is very similar to other comparable PHJ device structures.[26–29] The improved photovoltaic performance of the perovskite devices made from

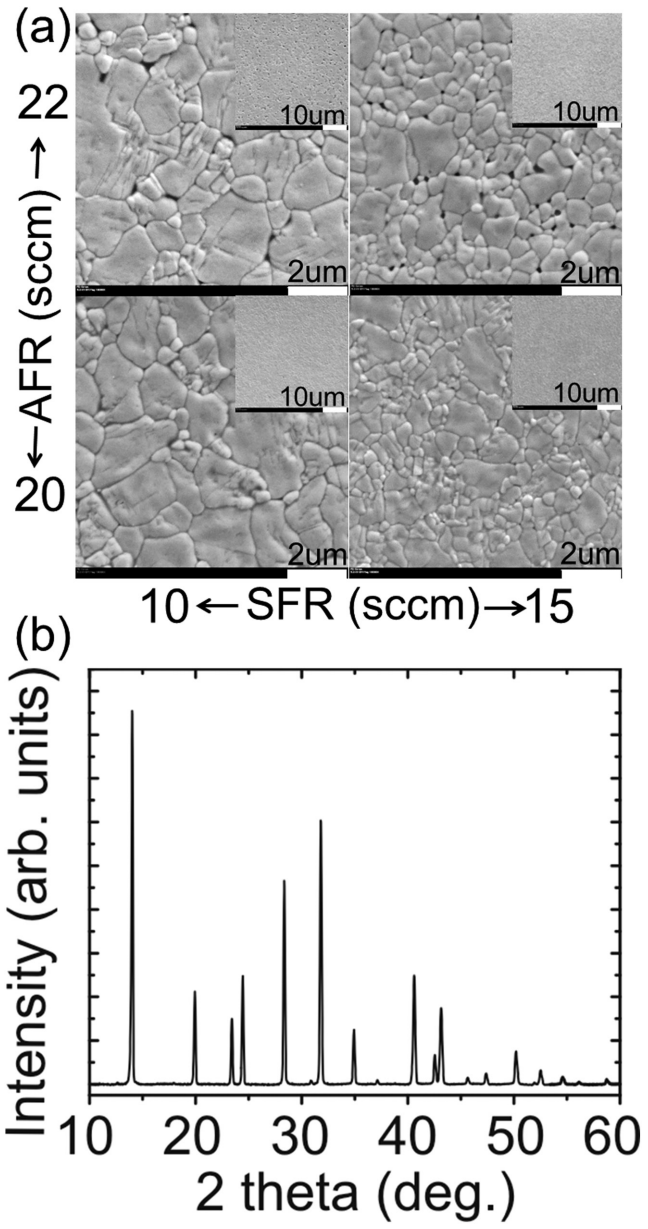

Figure 6. a) Top-view SEM images of the AJ printed perovskite films fabricated from nanoporous PbI_2 layer on glass/ITO/PEDOT:PSS surface with 2 mol% NaI additive in the CH_3NH_3I ink. b) A representative XRD pattern of one of those films.

a nanoporous PbI_2 layer by the additive enhanced route may be attributed to the full conversion of PbI_2 to $CH_3NH_3PbI_3$ and reduced recombination of photogenerated charge carriers at much smaller grain boundary areas in large crystalline domains of perovskite.[29,30] It is notable that the perovskite cells fabricated by AJP exhibit very narrow distribution of device performances compared to those made by a fully spin-coating process, indicating that the fabrication steps can be more reproducibly controlled using AJP. Taken together, these results unveil the capability of AJP for producing perovskite films having excellent morphology and compositional purity via the introduction of an AJP process.

2.3. Perovskite Direct Write on a Curved Substrate

Finally, we utilize this direct-write printing of the perovskite active layer to write an array of curved stripes on a hemispherical surface in order to demonstrate true, 3D printing capability. Designing nonconventional fabrication methods for solar cell manufacturing directly on the surface of arbitrary 3D objects could enable numerous embedded structural power applications with forms varying from self-powered robotics and zero-fuel ultra-lightweight aerial vehicles to energy-efficient smart buildings to wearable electronics.[31–34] To date, a transfer process of fully manufactured solar panels has been primarily used to conform to nonplanar form factors of 3D objects.[35,36] A fully automated solar cell production technology based on additive printing of component materials right onto the targeted structures could be advantageous due to its nonsubtractive nature, easy adaptability to different form factors, and possible elimination of traditional module installation cost.

As a proof-of-concept demonstration of producing printed thin-film perovskite films on nonplanar surfaces, a PbI_2 ink was aerosol jet deposited directly onto an ITO/PEDOT:PSS coated polyethylene terephthalate (PET) substrate attached to a hemispherical base surface to form the PbI_2 film (**Figure 8**a,b) (see methods in experimental section). The three axes of motion control (XY for the substrate and Z for the print head) in the printer permit automated nonplanar deposition where a constant working distance can be maintained throughout the deposition process. This is facilitated by the intrinsically collimated aerosol stream where working distances can be varied between 2 and 10 mm with negligible loss in feature fidelity.

After depositing the PbI_2 layer, MAI can be aerosol jet deposited precisely onto the previous layer using the fiducial alignment routines (Figure 8c). Here, the film is ultimately transformed to $CH_3NH_3PbI_3$ perovskite after the mist–solid crystallization process as discussed earlier. After nonplanar deposition and perovskite transformation, the PET-supported samples are removed from the hemispherical support and are laid flat in order to fabricate complete solar cells in a planar PET/ITO/PEDOT:PSS/perovskite/PCBM/C_{60}/Al structure. These devices deliver PCEs as high as 5.4% with a V_{oc} of 870 mV, a J_{sc} of 11.7 mA cm^{-2} and a FF of 53%. Such a notable PCE at the very initial stage of the technology development indicates exciting opportunities for further process optimization and also provides a wider view of pursuing 3D aerosol-jet printing systems for designing entirely new thin-film device fabrication rules and augmenting solar cell manufacturing as a whole.

3. Conclusions

We have successfully implemented automation in hybrid perovskite film fabrication and have presented a systematic comprehensive study on mitigating defects of $CH_3NH_3PbI_3$ film growth via a mist–solid crystallization process. This approach enables reproducible fabrication of high-quality, printed thin-film perovskite with tailored composition, morphology and electronic properties suitable for the "lab-to-fab" technology transition. Using a relatively small concentration of NaI additive in the precursor ink, highly crystalline, continuous and

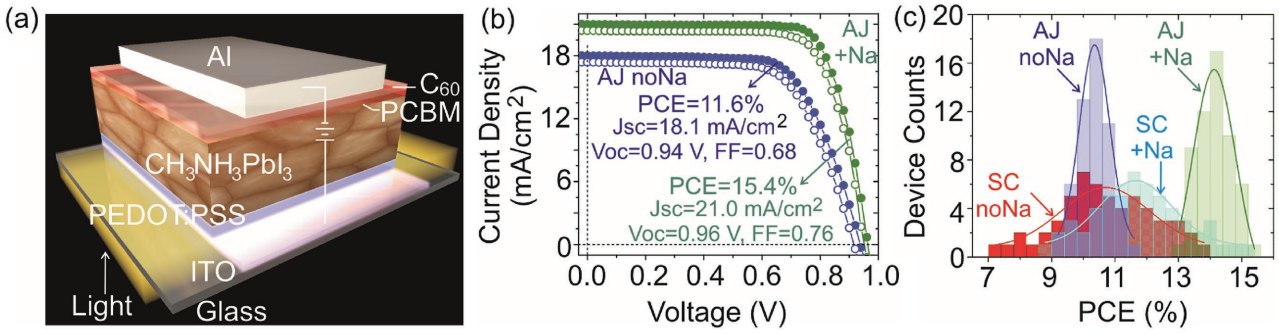

Figure 7. a) Planar heterojunction solar cell device structure studied in this work. b) *J–V* characteristics of best performing devices based on defect-mitigated (AJ printed) perovskite layer by AJ printing of CH_3NH_3I ink with and without NaI additive. Open circles: forward scan, closed circles: reverse scan. c) Distribution of device performance for spin coated (SC) and AJ printed perovskite solar cell devices with and without NaI additive. Gaussian fits for histograms of each device types are overlaid in the same graph.

large grained phase-pure perovskite thin films are produced by aerosol-jet printing under an ambient atmosphere. These results contributed significantly to achieving outstanding solar cell PCEs up to 15.4% with very narrow performance distribution. The printing process for preparing such perovskite films is potentially scalable and less labor intensive as compared to conventional two-step solution deposition processes. It may be possible that a fully aerosol-jet printed perovskite solar cell can be achieved at low-temperature based on ligand-engineering and other solution processable carrier transport layers.[37] For example, NiO_x,[38] SnO_2,[39] and PEDOT:PSS[40] inks can be used as the carrier transport layers by the AJP technique. Endowed with high-fidelity and process robustness, the applicability of this approach is likely to be extended to large areas and to the growing family of perovskite semiconductors[41–43] where the integration of thin films into sophisticated architectures would lead to the production of a variety of optoelectronic devices such as light-emitting diodes, photodetectors, and sensors.[34,44–46] Furthermore, the direct-printed 5.4% efficient solar cell on a curved surface marks the first demonstration in the field of printed photovoltaics. While further improvement of device performance is expected with additional process engineering and judicious materials selection, the ability of AJP to fabricate printed thin films directly onto 3D objects expands the flexibility of substrate selection and opens up new avenues for innovative device design and manufacturing processes.

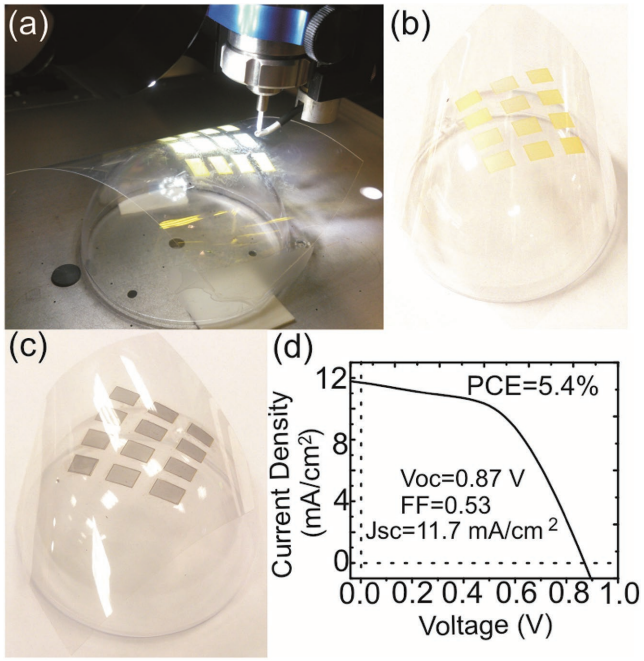

Figure 8. a) Snapshot of the direct printing process of perovskite semiconductor on a hemispherical surface during aerosol-jet operation. Photographs of AJ printed b) PbI_2 and c) $CH_3NH_3PbI_3$ on PET/ITO/PEDOT:PSS surface attached to a hemispherical substrate. d) *J–V* characteristics of a perovskite solar cell made by direct printing of the photoactive layer on the hemisphere in a PET/ITO/PEDOT:PSS/$CH_3NH_3PbI_3$/PCBM/C60/Al type PHJ device structure.

4. Experimental Section

Materials and Synthesis: Methylammonium lead tri-iodide perovskite precursors, PbI_2 (99.999% purity) was purchased from Sigma-Aldrich and methylammonium iodide (CH_3NH_3I, MAI) was synthesized according to a previously reported procedure.[47] In summary, 30 mL of hydroiodic acid (57% in water, Aldrich) was reacted with 27.9 mL of methylamine (40% in methanol) in a 250 mL round-bottom flask at 0 °C for 2 h with continuous stirring. The resultant white precipitate was recovered by evaporating the solution at 50 °C for 1 h in a rotary evaporator. The product was dissolved in ethanol, recrystallized using diethyl ether, and dried at 60 °C under vacuum for 24 h.

PEDOT:PSS was purchased from Heraeus Materials Technology (Dayton, OH) and used as received. "X" prepatterned ITO glass substrates (sheet resistance of 15 $\Omega\ \square^{-1}$) were purchased from Luminescence Technology Corp. (Taiwan). ITO-coated PET substrates (surface resistivity of 60 ohm per square), anhydrous isopropanol, dimethyl sulfoxide, dimethyl formamide, dichlorobenzene and sodium iodide were obtained from Sigma-Aldrich. $PC_{71}BM$ and C_{60} were purchased American Dye Source, Inc. (Baie D'Urfe, QC). For thermal evaporation, aluminum (99.999% purity) pellets from Kurt J. Lesker Co. (Jefferson Hills, PA) were used.

Characterizations and Measurements: J–V characterization of the photovoltaic cells were performed inside a M-Braun Lab-Master glovebox using a Keithley 2410 under a 100 mW cm^{-2} simulated AM 1.5G illumination (Oriel 91160 solar simulator). Before each *J–V* measurement test, samples were continuously soaked for 10 min under the same simulated light. A 2 s delay was applied before each measurement point during the photocurrent characterization (scan rate of 10 mV s^{-1}).

Incident-photon-conversion efficiencies (IPCEs) or external quantum efficiencies (EQE) were characterized using an Oriel model QE-PV-SI instrument equipped with a NIST-certified Si diode. Monochromatic light was generated from an Oriel 300 W lamp. A Bruker Dektak XT profilometer (Billerica, MA) was used for all thickness measurements and a FEI Sirion scanning electron microscopy for all surface morphology investigations. A Rigaku-D/Max-B X-ray diffractometer with Bragg-Brentano parafocusing geometry was used to acquire the XRD patterns. Optical absorption spectra were obtained using an Agilent Cary 5000 spectrometer (Santa Clara, CA) in the transmission mode. The time-resolved photoluminescence (TRPL) measurements were done films on glass by an EDINBURGH INSTRUMENT (OB920) with an excitation wavelength of 375 nm from a pulsed laser. Thin metal (Al) and C_{60} were deposited by using a BOC EDWARDS (Auto 500 system) thermal evaporator integrated to a nitrogen-filled glove box where all the postprocessing steps of the aerosol-jet deposited perovskite films were carried out.

Fabrication of Thin-Film Perovskite Solar Cells: All traditional, planar thin-film perovskite solar cell devices were fabricated on patterned ITO glass (Sheet resistance of 15 $\Omega\ \square^{-1}$) substrates. On the day of deposition, the ITO glass substrates were cleaned sequentially by sonicating with detergent, deionized water, acetone, and IPA, followed by drying with high flow of nitrogen and UV-ozone treatment for 20 min. Filtered (0.45 µm PVDF filter) PEDOT:PSS was spin coated onto the clean ITO glass substrates at 3000 rpm for 60 s and then dried on a ceramic hot-plate at 160 °C for 15 min in ambient atmosphere. Thereafter, $CH_3NH_3PbI_3$ active layer was fabricated by a two-step sequential deposition method with the help of a commercial aerosol-jet printer. First, hot PbI_2 [dissolved in anhydrous DMF at 75 °C, 400 mg mL^{-1} concentration] solution was spun on the top of the glass/ITO/PEDOT:PSS by a spin-coater at a spin rate of 6000 rpm for 35 s and the resulting PbI_2 layer was dried in a closed container for 0 to 12 min duration at room temperature followed by a mild annealing at 80 °C for 10 min on a hot plate. The presence of residual DMF solvent in the film before this annealing step promotes crystal growth and the longer the growth time (hold time of the film in the closed container immediately after spin-coating) the larger is the crystal growth resulting in formation of nanoporous structures in the film.[24] The extent of nanopore generation can be quenched by annealing the film immediately after spin-coating. Thus PbI_2 films with different microstructures were obtained at this stage by drying the spin-coated layers differently. The CH_3NH_3I aerosol mist was generated from a solution containing 2 wt% CH_3NH_3I in IPA:DMF (1:3, v/v) mixture by an aerosol-jet printer using ultrasonic transduction and was subsequently deposited onto the solid PbI_2 layer in air with variable atomizer and sheath flow rates (nozzle diameter: 150 µm, x–y stage movement speed: 30 mm s^{-1}, relative humidity below 30%). The mechanism of aerosol-jet deposition is quite different from other solution-based deposition processes. Using the MAI formulation in IPA, commonly used in spin-coating process,[29] we encountered serious issues with MAI printing, which involves rapid and uncontrollable MAI deposition. MAI in IPA:DMF (1:3, v/v) mixture enables exquisite control over the MAI printing process. For additive-based printing, a small amount (2 mol%) of sodium iodide is added in the CH_3NH_3I formulation (in IPA:DMF). The platen temperature was maintained at 70 °C throughout the printing process. The timing diagram of the printing process and the line pattern (at 10 µm spacing) of the jetted aerosol mist are shown in Figure 1c,d, respectively. Printed PbI_2 layer was made similarly by the same aerosol-jet printer from a 10 wt% PbI_2 solution in DMSO. PbI_2 layer rapidly changed its color from light yellow to dark brown at predefined square/rectangular areas after exposure to the sufficient amount of aerosolized CH_3NH_3I mist. Next, the printed samples were then taken into a N_2-filled glove box where remaining device fabrication and measurement steps were carried out. To enhance crystallization and perovskite conversion, the samples were annealed on a hot plate at 100 °C for 80 min with a drop of DMF covered with a glass lid. After the annealing step, a thin layer of $PC_{71}BM$ (20 mg mL^{-1} in dichlorobenzene) was deposited on the top of the $CH_3NH_3PbI_3$ layer by spin-coating and then solvent annealed (in dichlorobenzene rich environment) at room temperature overnight. Ultimately, the device was finished by thermal evaporation of C_{60} (30 nm) and Al (150 nm). The active area of each device is 0.1 cm^2, measured by the overlap of top Al electrode and ITO. In order to avoid the overestimation of photocurrent density by the optical piping effect (any cross talking between two adjacent cells), device active area was defined by careful mechanical scribing by a sharp razor blade together with the use of an optical aperture. The performance of these devices were compared to devices made from traditional two-step spin-coated perovskite layer in air where the respective MAI inks (4 wt% in anhydrous IPA with and without additive) were dripped onto the similar PbI_2 layer during spinning at high rate (6000 rpm). All other fabrication steps were kept same.

For aerosol-jet printing of perovskite on a curved surface, first PEDOT:PSS was deposited on a precleaned and UV-ozone treated PET/ITO substrate by spin-coating. After the coating was completely dried by baking at 160 °C for 15 min, the coated PET substrate was wrapped around a hemispherical substrate and glued as shown in Figure 8b. Using AutoCAD design files, PbI_2 and CH_3NH_3I were sequentially deposited onto this curved substrate, directly without any disassembly step by the aerosol-jet printer. Then after detaching the coated PET from the hemisphere and conforming to a flat surface, the stacked PET/ITO/PEDOT:PSS/PbI_2/CH_3NH_3I layers were taken inside a glove box where full solar cells were constructed afterward using the same processing protocols and device geometry as the reference cells made on the ITO-coated glass. Here, the curved piece is flattened solely to measure the efficiency of the device using standard measurement equipment. During the full device fabrication, wherever spin coating steps were applied for thin-film deposition (i.e., PEDOT:PSS and PCBM), the bottom of the PET substrate was attached to a flat, rigid base (e.g., glass) to prevent distortion of the flexible PET. After spin-coating, the PET substrate was carefully peeled off from the base. Irrespective of the substrate, *J–V* characteristics of all fabricated devices were measured similarly using a Keithley 2410 source measure unit under a simulated AM 1.5G spectrum under N_2 inert atmosphere.

Supporting Information

Supporting Information is available from the Wiley Online Library or from the author.

Acknowledgements

This work was supported by the Air Force Office of Scientific Research (AFSOR).

Conflict of Interest

The authors declare no conflict of interest.

Keywords

aerosol-jet, defect mitigation, direct write, perovskite semiconductor, solar cells

Received: April 26, 2017
Revised: June 4, 2017
Published online:

[1] D. Stüwe, D. Mager, D. Biro, J. G. Korvink, *Adv. Mater.* **2015**, *27*, 599.
[2] Q. Chen, N. De Marco, Y. M. Yang, T.-B. Song, C.-C. Chen, H. Zhao, Z. Hong, H. Zhou, Y. Yang, *Nano Today* **2015**, *10*, 355.

[3] W. Zhang, G. E. Eperon, H. J. Snaith, *Nat. Energy* **2016**, *1*, 16048.
[4] T. J. Jacobsson, J.-P. Correa-Baena, M. Pazoki, M. Saliba, K. Schenk, M. Grätzel, A. Hagfeldt, *Energy Environ. Sci.* **2016**, *9*, 1706.
[5] K. Hwang, Y. S. Jung, Y. J. Heo, F. H. Scholes, S. E. Watkins, J. Subbiah, D. J. Jones, D. Y. Kim, D. Vak, *Adv. Mater.* **2015**, *27*, 1241.
[6] R. Po, A. Bernardi, A. Calabrese, C. Carbonera, G. Corso, A. Pellegrino, *Energy Environ. Sci.* **2014**, *7*, 925.
[7] T.-B. Song, Q. Chen, H. Zhou, C. Jiang, H.-H. Wang, Y. M. Yang, Y. Liu, J. You, Y. Yang, *J. Mater. Chem. A* **2015**, *3*, 9032.
[8] T. Salim, S. Sun, Y. Abe, A. Krishna, A. C. Grimsdale, Y. M. Lam, *J. Mater. Chem. A* **2015**, *3*, 8943.
[9] A. Sharenko, M. F. Toney, *J. Am. Chem. Soc.* **2015**, *138*, 463.
[10] Z. Yang, C. C. Chueh, F. Zuo, J. H. Kim, P. W. Liang, A. K.-Y. Jen, *Adv. Energy Mater.* **2015**, *5*, 1500328.
[11] Y. Deng, E. Peng, Y. Shao, Z. Xiao, Q. Dong, J. Huang, *Energy Environ. Sci.* **2015**, *8*, 1544.
[12] A. T. Barrows, A. J. Pearson, C. K. Kwak, A. D. F. Dunbar, A. R. Buckley, D. G. Lidzey, *Energy Environ. Sci.* **2014**, *7*, 2944.
[13] S. Das, B. Yang, G. Gu, P. C. Joshi, I. N. Ivanov, C. M. Rouleau, T. Aytug, D. B. Geohegan, K. Xiao, *ACS Photonics* **2015**, *2*, 680.
[14] H. Ishihara, W. Chen, Y. C. Chen, S. Sarang, N. De Marco, O. Lin, S. Ghosh, V. Tung, *Adv. Mater. Interfaces* **2016**, *3*, 1500762.
[15] Z. Wei, H. Chen, K. Yan, S. Yang, *Angew. Chem., Int. Ed.* **2014**, *126*, 13455.
[16] D. Vak, K. Hwang, A. Faulks, Y. S. Jung, N. Clark, D. Y. Kim, G. J. Wilson, S. E. Watkins, *Adv. Energy Mater.* **2015**, *5*, 1401539.
[17] T. M. Schmidt, T. T. Larsen-Olsen, J. E. Carlé, D. Angmo, F. C. Krebs, *Adv. Energy Mater.* **2015**, *5*, 1500569.
[18] Perovskite Solar Cells Technology Improving, Commercialization Likely in 2019, https://cleantechnica.com/2016/05/16/lux-research-perovskite-solar-cells-technology-improving-commercialization-likely-2019/ (accessed: September 2016).
[19] Aerosol Jet Technology for 3D Printed Electronics, http://www.optomec.com/printed-electronics/aerosol-jet-technology/ (accessed: September 2016).
[20] F. Hao, C. C. Stoumpos, Z. Liu, R. P. Chang, M. G. Kanatzidis, *J. Am. Chem. Soc.* **2014**, *136*, 16411.
[21] J.-H. Im, I.-H. Jang, N. Pellet, M. Grätzel, N.-G. Park, *Nat. Nanotechnol.* **2014**, *9*, 927.
[22] C. C. Stoumpos, C. D. Malliakas, M. G. Kanatzidis, *Inorg. Chem.* **2013**, *52*, 9019.
[23] H. Zhang, J. Mao, H. He, D. Zhang, H. L. Zhu, F. Xie, K. S. Wong, M. Grätzel, W. C. Choy, *Adv. Energy Mater.* **2015**, *5*, 1501354.
[24] T. Liu, Q. Hu, J. Wu, K. Chen, L. Zhao, F. Liu, C. Wang, H. Lu, S. Jia, T. Russell, R. Zhu, Q. Gong, *Adv. Energy Mater.* **2016**, *6*, 1501890.
[25] C.-G. Wu, C.-H. Chiang, Z.-L. Tseng, M. K. Nazeeruddin, A. Hagfeldt, M. Grätzel, *Energy Environ. Sci.* **2015**, *8*, 2725.
[26] S. Bag, M. F. Durstock, *ACS Appl. Mater. Interfaces* **2016**, *8*, 5053.
[27] S. Bag, M. F. Durstock, *Nano Energy* **2016**, *30*, 542.
[28] Y. Shao, Z. Xiao, C. Bi, Y. Yuan, J. Huang, *Nat. Commun.* **2014**, *5*, 5784.
[29] Z. Xiao, Q. Dong, C. Bi, Y. Shao, Y. Yuan, J. Huang, *Adv. Mater.* **2014**, *26*, 6503.
[30] T. Leijtens, S. D. Stranks, G. E. Eperon, R. Lindblad, E. M. J. Johansson, I. J. McPherson, H. Rensmo, J. M. Ball, M. M. Lee, H. J. Snaith, *ACS Nano* **2014**, *8*, 7147.
[31] Solar Impulse Clean Technologies to Fly Around the World, https://www.solarimpulse.com/ (accessed: September 2016).
[32] S. Yoon, S. Tak, J. Kim, Y. Jun, K. Kang, J. Park, *Build. Environ.* **2011**, *46*, 1899.
[33] Wearable Solar, http://wearablesolar.nl/ (accessed: September 2016).
[34] W. Xu, H. Cho, Y. H. Kim, Y. T. Kim, C. Wolf, C. G. Park, T. W. Lee, *Adv. Mater.* **2016**, *28*, 5916.
[35] Y. Wang, S. Bai, L. Cheng, N. Wang, J. Wang, F. Gao, W. Huang, *Adv. Mater.* **2016**, *28*, 4532.
[36] M. Kaltenbrunner, G. Adam, E. D. Głowacki, M. Drack, R. Schwödiauer, L. Leonat, D. H. Apaydin, H. Groiss, M. C. Scharber, M. S. White, *Nat. Mater.* **2015**, *14*, 1032.
[37] H. Zhang, J. Cheng, D. Li, F. Lin, J. Mao, C. Liang, A. K.-Y. Jen, M. Grätzel, W. C. H. Choy, *Adv. Mater.* **2017**, *29*, 1604695.
[38] H. Zhang, J. Cheng, F. Lin, H. He, J. Mao, K. S. Wong, A. K.-Y. Jen, W. C. H. Choy, *ACS Nano* **2016**, *10*, 1503.
[39] Z. Zhu, Y. Bai, X. Liu, C.-C. Chueh, S. Yang, A. K.-Y. Jen, *Adv. Mater.* **2016**, *28*, 6478.
[40] D. K. Mohamad, J. Griffin, C. Bracher, A. T. Barrows, D. G. Lidzey, *Adv. Energy Mater.* **2016**, *1*, 1600994.
[41] H. Tsai, W. Nie, J.-C. Blancon, C. C. Stoumpos, R. Asadpour, B. Harutyunyan, A. J. Neukirch, R. Verduzco, J. J. Crochet, S. Tretiak, *Nature* **2016**, *536*, 312.
[42] C. C. Stoumpos, M. G. Kanatzidis, *Acc. Chem. Res.* **2015**, *48*, 2791.
[43] C. C. Stoumpos, M. G. Kanatzidis, *Adv. Mater.* **2016**, *28*, 5778.
[44] S. Chen, C. Teng, M. Zhang, Y. Li, D. Xie, G. Shi, *Adv. Mater.* **2016**, *28*, 5969.
[45] H. Zhu, Y. Fu, F. Meng, X. Wu, Z. Gong, Q. Ding, M. V. Gustafsson, M. T. Trinh, S. Jin, X. Zhu, *Nat. Mater.* **2015**, *14*, 636.
[46] S. Yakunin, M. Sytnyk, D. Kriegner, S. Shrestha, M. Richter, G. J. Matt, H. Azimi, C. J. Brabec, J. Stangl, M. V. Kovalenko, *Nat. Photonics* **2015**, *9*, 444.
[47] L. Etgar, P. Gao, Z. Xue, Q. Peng, A. K. Chandiran, B. Liu, M. K. Nazeeruddin, M. Grätzel, *J. Am. Chem. Soc.* **2012**, *134*, 17396.

